Combining First and Second Order Continuity Constraints in Ultrasound Elastography

Md Ashikuzzaman, *Student Member*, *IEEE*, Ali Sadeghi-Naini, *Senior Member*, *IEEE*, Abbas Samani, *Senior Member*, *IEEE*, and Hassan Rivaz, *Senior Member*, *IEEE*

***Abstract*—Ultrasound elastography is a prominent non-invasive medical imaging technique which estimates tissue elastic properties to detect abnormalities in an organ. A common approximation to tissue elastic modulus is tissue strain induced after mechanical stimulation. To compute tissue strain, ultrasound radio-frequency (RF) data can be processed using energy-based algorithms. These algorithms suffer from ill-posedness to tackle. A continuity constraint along with the data amplitude similarity is imposed to obtain a unique solution to the time-delay estimation (TDE) problem. Existing energy-based methods exploit the first-order spatial derivative of the displacement field to construct a regularizer. This first-order regularization scheme alone is not fully consistent with the mechanics of tissue deformation while perturbed with an external force. As a consequence, state-of-the-art techniques suffer from two crucial drawbacks. First, the strain map is not sufficiently smooth in uniform tissue regions. Second, edges of the hard or soft inclusions are not well-defined in the image. Herein, we address these issues by formulating a novel regularizer taking both first- and second-order derivatives of the displacement field into account. The second-order constraint, which is the principal novelty of this work, contributes both to background continuity and edge sharpness by suppressing spurious noisy edges and enhancing strong boundaries. We name the proposed technique SOUL- Second Order Ultrasound eLastography. Comparative assessment of qualitative and quantitative results shows that SOUL substantially outperforms three recently developed TDE algorithms called Hybrid, GLUE and MPWC-Net++. SOUL yields 27.72%, 62.56% and 81.37% improvements of signal-to-noise ratio (SNR) and 72.35%, 54.03% and 65.17% improvements of contrast-to-noise ratio (CNR) over GLUE with data pertaining to simulation, phantom and *in vivo* tissue, respectively. The SOUL code can be downloaded from code.sonography.ai..**

***Index Terms*—Ultrasound elastography, Second order regularization, Boundary sharpness, Background smoothness, Regularized optimization, Global time delay estimation.**

I. Introduction

Being non-invasive, portable and easy-to-use, ultrasound is one of the most commonly used medical imaging modalities. This modality has been employed in the assessment of thyroid, breast, abdomen, prostate, kidney and vasculature. Ultrasound elastography is an emerging technique that characterizes tissue elasticity, which has numerous applications in medical diagnosis and intervention since certain pathologies lead to tissue structure alteration that manifest into tumors and benign lesions that have a significantly different mechanical properties compared to healthy tissue. Over the last three decades, elastography has been incorporated in breast tissue classification [1]–[4], liver health monitoring [5], guiding ablation [6], [7], cardiac imaging [8]–[12], and detection of abnormalities in vessels [13]–[18], prostate [19] and kidney [20]. This work is aimed at quasi-static elastography, which involves calculation of displacement field between pre- and post-deformed radio-frequency (RF) frames acquired during slow deformation of the interrogated tissue. The displacement map is calculated using a time-delay estimation (TDE) (alternatively known as speckle tracking) technique, and is subsequently spatially differentiated to obtain the strain map. This map is considered a good approximation to tissue elastic modulus as it can discern tissue abnormalities by a color contrast between the healthy and diseased tissues.

The success of ultrasound elastography is highly dependent on the pivotal task of TDE. Three different lines of works are available in the literature which accomplish this non-trivial task of speckle tracking. The mostly used approach is known as the window-based or block-matching technique [21]–[24] which entails dividing the RF data into several data segments and imposing hard constraint of displacement equality among all samples in a certain window. The time-delay of each window is calculated using a similarity metric such as normalized cross-correlation (NCC) [24] or zero-phase crossing [23]. Optimal performance of window-based techniques depends on the proper selection of window size and the degree of overlap between the adjacent windows. A large window leads to a smooth displacement map sacrificing the resolution, whereas a high-resolution TDE can be obtained by incorporating a small data window [25], [26]. However, a small-sized data window amplifies the estimation noise which can be handled by post-processing techniques such as median filtering. However, such post-processing techniques do not utilize the continuity constraints to improve TDE in a unified fashion.

Recently, machine learning-based TDE techniques [27]–[31] have been proposed which require extensive amount of training data for accomplishing the task of speckle tracking. In addition, dictionary learning techniques have been investigated for fast and better displacement estimation [32], [33]. Furthermore, robust principal component analysis (RPCA) has been proposed as a noise-reduction step of ultrasound elastography [34]. Despite the primary success in TDE, all proposed machine learning-based algorithms share a common

Md Ashikuzzaman and Hassan Rivaz are with the Department of Electrical and Computer Engineering, Concordia University, Montreal, QC, H3G 1M8, Canada. Email: m_ashiku@encs.concordia.ca and hrivaz@ece.concordia.ca

Ali Sadeghi-Naini is with the Department of Electrical Engineering and Computer Science, York University, Toronto, ON, M3J 1P3, Canada. Email: asn@eecs.yorku.ca

Abbas Samani is with the Department of Electrical and Computer Engineering and the Department of Medical Biophysics, The University of Western Ontario, London, ON, N6A 3K7, Canada. Email: asamani@uwo.ca

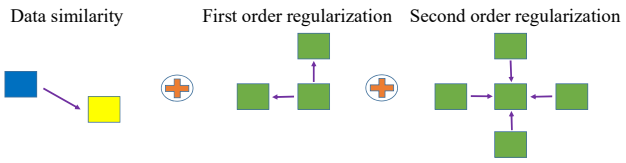

Fig. 1: A depiction of the proposed cost function. Blue and yellow represent RF signal amplitudes of the two images, and green represents displacement estimates.

drawback which is excessive data-dependency.

The last mainstream class of TDE technique is referred to as regularized optimization-based or energy-based algorithms [35]–[42]. A penalty function consisting of data and regularization term is optimized in this line of work to estimate the time delay. Energy-based algorithms are less-sensitive to noise due to the regularization constraint incorporated in the cost function. The assumption of displacement continuity aligns with the physics of tissue deformation, and is an essential component in the energy-based approach. Because data similarity constraint alone yields more than one displacement solutions for a particular sample due to the non-unique nature of RF data amplitude. Mathematically, this phenomenon is linked to the situation of having more variables than equations which makes TDE an ill-posed problem. The $l2$ norm of spatial [5], [37], [38] and temporal [38] continuity terms have been taken into account in recent works. The $l1$ norm regularization which is otherwise known as the total variation regularization has also been proposed in [43] to tackle the over-smoothing possibly introduced by earlier techniques. All of the aforementioned algorithms consider only the first-order derivative of the displacement field to construct the regularization term. This first-order continuity term often generates strain image with blurred inclusion-background boundary. In addition, it fails to sufficiently denoise the displacement or strain map. One possible solution to this issue is increasing the continuity weight. However, this aggressive step leads to substantial degradation of image contrast.

To resolve the aforementioned issues, in this paper, we develop a novel energy-based elastography technique where both first- and second-order derivatives of the displacement fields have been considered to formulate the penalty function (see Fig. 1). Our contribution is driven by the fact that the second-order image derivative enhances the strong boundaries suppressing the weak edges which often originate from the acquisition or estimation noise. Therefore, our assumption is that incorporation of the second-order regularization in the cost function leads to a higher level of continuity, keeping the visual contrast intact. The Laplacian of the displacement field has previously been used in [44] as a post-processing step. However, this work proposes a unified technique where the second-order condition is embedded within the penalty function along with the first-order continuity constraint. It is worth mentioning that Li *et al.* incorporated a second-order continuity constraint in [14]. However, [14] is especially designed for vascular elastography and combines discrete cosine transform (DCT) based sparsity constraint with optical flow-based approach to devise a direct strain estimation framework. On the contrary, we propose a generalized displacement tracking scheme which can be used in different applications, while it efficiently utilizes Gauss-Newton optimization technique to refine the initial TDE obtained by Dynamic Programming [45]. We name our technique SOUL: **S**econd **O**rder **U**ltrasound e**L**astography. SOUL has been validated with simulation, phantom and *in vivo* liver datasets. We have released the SOUL code at code.sonography.ai similar to our recent work [38], [46], [47].

II. Simulation and Data Acquisition

A. Simulation Datasets

In this work, we have used five different simulation datasets for validation. The first dataset was simulated from a uniform phantom. The second simulation data was generated from a phantom with four layers representing different elasticity levels. The third data was generated from a simulated phantom which contains a thin layer with higher elasticity. The fourth dataset was produced from a homogeneous phantom containing a layer with slightly higher stiffness. The last dataset was obtained from homogeneous phantom with a soft inclusion. Pre- and post-deformed RF frames from all phantoms were simulated using the commonly used software package Field II [48]. A single-focused acquisition scheme was incorporated setting the center frequency, sampling rate, number of active elements, transducer height and width to 7.27 MHz, 40 MHz, 64, 5 mm and 0.2 mm, respectively. The transmit focus was set to 12.5 mm for the uniform and soft-inclusion phantoms and 20 mm for the other three phantoms.

1) Uniform Phantom: We designed a tissue phantom with uniform elastic properties. The phantom was compressed axially using closed form equation of deformation. For this uniform phantom, a parabolic displacement field was considered where the strain linearly decays (from 0.02 to 0) with depth. This displacement profile was designed to simulate a nonlinear medium wherein the top layers absorb more displacement.

2) Four-layer Phantom: A homogeneous phantom with a background elastic modulus of 20 kPa was generated. The phantom contains two hard homogenous layers with Young's moduli of 40 and 80 kPa. The phantom was compressed using closed form equations so that the bottom surface deforms by 4% of its original height. The equations describing the deformation model can be found in the Supplementary material of [38].

3) Thin-layer Phantom: A homogeneous phantom which includes a hard layer of 4 mm height was simulated. Young's moduli of background and inclusion were set to 20 kPa and 40 kPa, respectively. Closed form equations were used to compress the phantom so that the bottom surface deforms by 4% of the phantom's height.

4) Low-contrast Phantom: A homogeneous phantom with a slightly harder layer was simulated where Young's moduli of background and inclusion were set to 20 kPa and 22.86 kPa, respectively. The phantom was compressed utilizing closed form equations to achieve a 4% deformation of the bottom surface.

Algorithm 1: Workflow of the SOUL algorithm

Input: Pre- and post-deformed RF frames I_1 and I_2
Output: Axial strain map

1 Estimate a and l: Integer displacement field obtained by Dynamic Programming (DP) [45];
2 Formulate C: The penalty function consisting of data, first- and second-order regularization terms (Eq. 4);
3 Analytically optimize the cost function C;
4 Estimate Δa and Δl: The refinement displacement field (Eq. 10);
5 Obtain the final displacement estimate by adding the refinement field to the DP initial guess;
6 Obtain the axial strain map by taking the spatial derivative of the axial displacement field

5) Soft-inclusion Phantom: A homogeneous phantom was designed which contains an easily deformable vein of diameter 8 mm in the middle. The Young's modulus of the background was set to 4 kPa. The phantom was compressed axially so that the bottom surface deforms by 1% of its original height. The displacements were estimated using the ABAQUS finite element package (Providence, RI).

B. Experimental Phantom Datasets

A breast elastography phantom (CIRS: Tissue Simulation & Phantom Technology, Norfolk, VA) with background and target elasticity moduli of 33 kPa and 56 kPa, respectively, was compressed using a linear stage. RF data were acquired from the aforementioned experimental phantom during compression with an Antares Siemens research ultrasound machine (Issaquah, WA) using a VF 10-5 linear array probe. The transmit and sampling frequencies were set to 6.67 and 40 MHz, respectively.

C. In vivo Liver Datasets

The *in vivo* datasets were acquired from two liver cancer patients undertaking open-surgical thermal ablation in Johns Hopkins Hospital. The RF ablation procedure was monitored by RITA Model 1500 XRF generator (Rita Medical Systems, Fremont, CA). The tissue compression was performed by pushing the ultrasound probe against the liver at a rate of approximately 2 compressions per second. RF frames were collected using the Antares Siemens research ultrasound system with the VF 10-5 linear array probe. The center frequency and the temporal sampling rate were set to 6.67 and 40 MHz, respectively. All data acquisition steps were carried out according to approved ethics protocol obtained from the Institutional Review Board. In addition, both patients provided written consent for this experimental study. Further details regarding this *in vivo* study can be found in [5].

III. Methods

Let $I_1(i,j)$ and $I_2(i,j)$, $1 \leq i \leq m$, $1 \leq j \leq n$ be two ultrasound RF frames collected from a tissue which is being deformed. Here, i and j denote the axial and lateral positions, respectively. Our aim is to estimate the strain map between I_1 and I_2. We first describe three previous techniques called Hybrid [3], MPWC-Net++ [47] and GLUE [37]. Then we outline the novelties and mathematical details of SOUL, the proposed technique.

A. Hybrid

Solid and fluid-filled lesions are detected using NCC and speckle-tracking techniques, respectively. Hybrid combines the tracking results obtained by both techniques. Based on three criteria, the presence and locations of fluid-filled lesions are determined. The strain estimates for solid lesions are obtained using modified direct average spectral strain estimation (DASSE) algorithm [49]. Neighboring samples are taken into account during strain estimation for intrinsic noise suppression. Further denoising is performed by applying a median filter on the strain image.

B. Modified Pyramidal Network (MPWC-Net++)

MPWC-Net [30] removes stride from PWC-Net [50] and utilizes this modified version to calculate optical flow between ultrasound RF frames. MPWC-Net++ [47] utilizes PWC-Net-IRR [51] and resolves the limitations of MPWC-Net by increasing the search range and reducing the strides. In addition, MPWC-Net++ increases the maximum allowance for displacement by tuning different parameters. Furthermore, it uses the imaginary part of the RF data instead of B-mode image as the network input.

C. Global Ultrasound Elastography (GLUE)

In GLUE, the initial axial and lateral displacement fields $a_{i,j}$ and $l_{i,j}$ are obtained from Dynamic Programming (DP) [45]. These initial estimates are refined by the fine-tuning fields $\Delta a_{i,j}$ and $\Delta l_{i,j}$ which are obtained by optimizing a non-linear cost function C_g consisting of data amplitude similarity and spatial continuity terms:

$$\begin{aligned} &C_g(\Delta a_{1,1},...,\Delta a_{m,n},\Delta l_{1,1},...,\Delta l_{m,n}) = \\ &\sum_{j=1}^{n}\sum_{i=1}^{m} D_I(i,j,a_{i,j},l_{i,j},\Delta a_{i,j},\Delta l_{i,j}) + R_g \end{aligned} \tag{1}$$

where D_I denotes data amplitude similarity and is defined as follows:

$$\begin{aligned} &D_I(i,j,a_{i,j},l_{i,j},\Delta a_{i,j},\Delta l_{i,j}) = \\ &[I_1(i,j) - I_2(i+a_{i,j}+\Delta a_{i,j}, j+l_{i,j}+\Delta l_{i,j})]^2 \end{aligned} \tag{2}$$

R_g denotes a spatial regularization term which penalizes the first-order derivative of the displacement field, with subscript g referring to GLUE. R_g is defined as follows:

$$\begin{aligned} R_g = &\sum_{j=1}^{n}\sum_{i=1}^{m}\{\alpha_1(a_{i,j}+\Delta a_{i,j}-a_{i-1,j}-\Delta a_{i-1,j})^2 \\ &+ \alpha_2(a_{i,j}+\Delta a_{i,j}-a_{i,j-1}-\Delta a_{i,j-1})^2 \\ &+ \beta_1(l_{i,j}+\Delta l_{i,j}-l_{i-1,j}-\Delta l_{i-1,j})^2 \\ &+ \beta_2(l_{i,j}+\Delta l_{i,j}-l_{i,j-1}-\Delta l_{i,j-1})^2\} \end{aligned} \tag{3}$$

where α_1, α_2 and β_1, β_2 denote the axial and lateral continuity weights, respectively.

D. Second Order Ultrasound Elastography (SOUL)

Like GLUE, the proposed technique SOUL obtains the initial displacement estimate from DP which is refined by optimizing a penalty function containing echo similarity and regularization terms. Both GLUE and SOUL share the same echo amplitude similarity term. As described in the previous subsection, the cost function in GLUE contains only a first-order regularization term which penalizes the first derivative of the displacement field. This first-order continuity constraint alone does not suffice to represent the mechanics of tissue deformation and therefore leads to a suboptimal noise suppression. By incorporating a second-order regularization term in the cost function, we show that substantially smoother strain image can be obtained without any loss of visual contrast between different mediums.

The penalty function C associated with SOUL is defined as:

$$\begin{aligned} &C(\Delta a_{1,1}, ..., \Delta a_{m,n}, \Delta l_{1,1}, ..., \Delta l_{m,n}) = \\ &\sum_{j=1}^{n}\sum_{i=1}^{m} D_I(i, j, a_{i,j}, l_{i,j}, \Delta a_{i,j}, \Delta l_{i,j}) + R_s \end{aligned} \tag{4}$$

where R_s denotes the novel regularization term which consists of three parts and is defined as follows:

$$R_s = \sum_{j=1}^{n} \gamma[a_{1,j} + \Delta a_{1,j}]^2 + R_1 + R_2 \tag{5}$$

The first part of R_s imposes a first-order regularizer on the first sample of each RF line with an assumption that the imaginary sample prior to the first sample exhibits a zero displacement. Here, γ is the spatial regularization weight for the first sample(s). R_1 and R_2 are the first and second-order continuity terms, respectively.

The first-order regularization term suppresses noise by minimizing the first derivative of displacement along two neighboring points, which is not backed by physics. This condition often leads to an underestimation of the displacement field [5], [38]. To tackle this issue, we formulate the first-order regularizer R_1 in an adaptive manner where $(disp_i - disp_{i-1} - \epsilon)^2$ is penalized instead of $(disp_i - disp_{i-1})^2$ [38]. Here, ϵ indicates the average difference between the displacement estimates of two neighboring samples. We define R_1 as:

$$\begin{aligned} R_1 = &\sum_{j=1}^{n}\sum_{i=1}^{m}\{\alpha_1(a_{i,j} + \Delta a_{i,j} - a_{i-1,j} - \Delta a_{i-1,j} - \epsilon_a)^2 \\ &+ \alpha_2(a_{i,j} + \Delta a_{i,j} - a_{i,j-1} - \Delta a_{i,j-1} - \epsilon_a)^2 \\ &+ \beta_1(l_{i,j} + \Delta l_{i,j} - l_{i-1,j} - \Delta l_{i-1,j} - \epsilon_l)^2 \\ &+ \beta_2(l_{i,j} + \Delta l_{i,j} - l_{i,j-1} - \Delta l_{i,j-1} - \epsilon_l)^2\} \end{aligned} \tag{6}$$

where ϵ_a and ϵ_l are calculated as:

$$\epsilon_a = \tfrac{a_m - a_1}{m-1}, \quad \epsilon_l = \tfrac{l_n - l_1}{n-1} \tag{7}$$

We define the second-order regularization term R_2 as follows:

$$\begin{aligned} R_2 = &\sum_{j=1}^{n}\sum_{i=1}^{m}\{\theta_1(a_{i-1,j} + \Delta a_{i-1,j} + a_{i+1,j} + \Delta a_{i+1,j} \\ &-2a_{i,j} - 2\Delta a_{i,j})^2 \\ &+ \theta_2(a_{i,j-1} + \Delta a_{i,j-1} + a_{i,j+1} + \Delta a_{i,j+1} - 2a_{i,j} \\ &- 2\Delta a_{i,j})^2 \\ &+ \lambda_1(l_{i-1,j} + \Delta l_{i-1,j} + l_{i+1,j} + \Delta l_{i+1,j} - 2l_{i,j} - 2\Delta l_{i,j})^2 \\ &+ \lambda_2(l_{i,j-1} + \Delta l_{i,j-1} + l_{i,j+1} + \Delta l_{i,j+1} - 2l_{i,j} - 2\Delta l_{i,j})^2\} \end{aligned} \tag{8}$$

where θ_1, θ_2 and λ_1, λ_2 denote the axial and lateral regularization parameters for the second-order constraint, respectively. While the adaptive feature of the first-order constraint encourages the strain to converge to the correct value, the second-order constraint aligns with tissue deformation physics and imposes continuity on strain. Therefore, first- and second-order constraints act complementarily to generate accurate and spatially smooth strain map.

1) Cost Function Optimization: Although the regularization term R_s is quadratic in terms of the unknowns, the data term contains non-linearity since the unknowns appear within the nonlinear function I_2. We perform a $2D$ Taylor series expansion of $I_2(i+a_{i,j}+\Delta a_{i,j}, j+l_{i,j}+\Delta l_{i,j})$ around $(i+a_{i,j})$ and $(j+l_{i,j})$ to make the cost function in Eq. 4 quadratic:

$$\begin{aligned} &I_2(i + a_{i,j} + \Delta a_{i,j}, j + l_{i,j} + \Delta l_{i,j}) \approx \\ &I_2(i + a_{i,j}, j + l_{i,j}) + \Delta a_{i,j} I^{'}_{2,a} + \Delta l_{i,j} I^{'}_{2,l} \end{aligned} \tag{9}$$

where $I^{'}_{2,a}$ and $I^{'}_{2,l}$ stand for the axial and lateral derivatives of I_2, respectively. We optimize the quadratic cost function in Eq. 4 by setting $\frac{\partial C_{i,j}}{\partial \Delta a_{i,j}} = 0$ and $\frac{\partial C_{i,j}}{\partial \Delta l_{i,j}} = 0$. After some analytic manipulation, we obtain the following linear system of equations:

$$(H + D + D_2)\Delta d = H_1 \mu - (D + D_2)d + b_s \tag{10}$$

where $d = [a_{1,1}, l_{1,1}, a_{1,2}, l_{1,2}, \ldots, a_{m,n}, l_{m,n}]^T$ is a vector of size $2mn \times 1$ which contains the DP initial estimates. The refinement displacement estimates are stacked in $\Delta d \in \mathbb{R}^{2mn \times 1}$ which is defined as: $\Delta d = [\Delta a_{1,1}, \Delta l_{1,1}, \Delta a_{1,2}, \Delta l_{1,2}, \ldots, \Delta a_{m,n}, \Delta l_{m,n}]^T$. Matrices H, H_1, D, D_2 and vectors μ and b_s have been defined partly in the Appendix and partly in the Supplementary Material.

The refinement displacement estimates stacked in Δd are obtained by solving Eq. 10. The fine-tuning field is added to the DP initial estimates to obtain the final displacement tensor. The axial displacement field is spatially differentiated using a least square estimator [52] to generate the axial strain image. The steps of the proposed technique have been given in Algorithm 1.

IV. Results

Five sets of simulation data, experimental phantom data and two sets of *in vivo* liver cancer data have been employed to examine the performance of the proposed technique SOUL compared to three recently developed elastography algorithms: Hybrid [3], a window-based technique, MPWC-Net++ [47], a

machine learning-based algorithm and GLUE [37], an energy-based technique. Along with qualitative results, four different quantitative metrics namely the edge spread function (ESF) over a vertical line, root-mean-square error (RMSE), signal-to-noise ratio (SNR) and contrast-to-noise ratio (CNR) have been used for performance assessment. RMSE is defined by the following equation.

$$\text{RMSE} = \sqrt{\frac{\sum_{j=1}^{n}\sum_{i=1}^{m}(\hat{s}_{i,j} - s_{i,j})^2}{mn}} \tag{11}$$

where $\hat{s}_{i,j}$ and $s_{i,j}$ denote the estimated and ground truth strains corresponding to the sample at (i, j). Elastographic SNR and CNR are defined as follows [53], [54]:

$$\text{SNR} = \frac{\bar{s_b}}{\sigma_b} \qquad \text{CNR} = \frac{C}{N} = \sqrt{\frac{2(\bar{s_b} - \bar{s_t})^2}{{\sigma_b}^2 + {\sigma_t}^2}} \tag{12}$$

where $\bar{s_b}$ and $\bar{s_t}$ stand for the mean strain values on background and target windows, respectively. σ_b and σ_t denote the standard deviations of the strain values corresponding to the background and target windows, respectively.

For both GLUE and SOUL, the regularization weights $\{\alpha_1, \alpha_2, \beta_1, \beta_2\}$ were set to $\{30, 6, 30, 6\}$, $\{5, 1, 5, 1\}$, $\{5, 1, 5, 1\}$, $\{5, 1, 5, 1\}$, $\{5, 1, 5, 1\}$, $\{5, 1, 5, 1\}$, $\{20, 1, 20, 1\}$ and $\{0.25, 0.003, 0.2, 0.002\}$ for uniform simulation phantom, four-layer simulation phantom, thin-layer simulation phantom, low-contrast simulation phantom, soft-inclusion simulation phantom, CIRS breast elastography phantom, *in vivo* liver datasets 1 and 2, respectively, unless otherwise specified. The second-order regularization parameters of the proposed technique SOUL namely $\{\theta_1, \theta_2, \lambda_1, \lambda_2\}$ were selected as certain multiples of the first-order weights $\{\alpha_1, \alpha_2, \beta_1, \beta_2\}$. For the uniform, four-layer, thin-layer and low-contrast simulation phantoms, the multiplying factor was set to 1000 which was reduced to 500 for the soft-inclusion simulation phantom. For all experimental datasets, the multiplying factor was set to 100. γ was set to 0.8 for the uniform simulation data, whereas it was set to 0.1 for the other four sets of simulation data and the experimental phantom data. For the *in vivo* experiments, γ was considered to be 0. The nearest neighbor factors were set to 3 for generating the results of the Hybrid method. For all four algorithms under discussion, the qualitative results corresponding to different settings were compared visually to obtain the optimal set of parameters.

A. Simulation Results

1) Uniform phantom: Fig. 2 shows the strain profile over one vertical line of the simulated uniform phantom. Both Hybrid and MPWC-Net++ follow the trend of the ground truth. However, they exhibit extensive variance around the true strain. Although the variance in GLUE is substantially less than that in Hybrid and MPWC-Net++, the issue is not fully resolved. To further reduce the variance, we increase the regularization in GLUE by 10 times. As expected, this strong regularization reduces the estimation variance. However, this improvement in variance is achieved by sacrificing some accuracy as the curve flattens and deviates substantially from the ground truth. Another interesting observation about GLUE is that it underestimates the strains corresponding to the first few samples of an RF line. This might stem from the suboptimal regularization of the first sample. As it is evident from the strain profile, SOUL yields the highest resemblance to the ground truth by resolving both of the issues pertaining to variance and underestimation of the border strains.

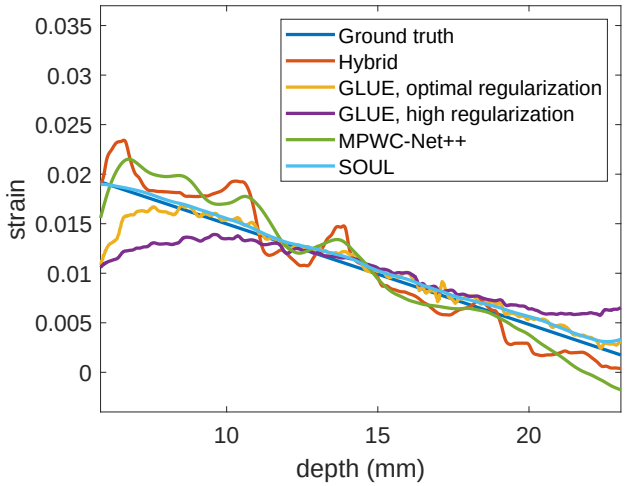

Fig. 2: Strain plot over a vertical line of the simulated uniform phantom with linearly decreasing strain profile.

TABLE I: RMSE associated with the strain images obtained from the simulated layer phantom with different realizations of scatterer position and amplitude.

	Realization 1	Realization 2	Realization 3
Hybrid	6.2×10^{-3}	5.7×10^{-3}	5.9×10^{-3}
GLUE	3.8×10^{-3}	3.8×10^{-3}	3.8×10^{-3}
MPWC-Net++	7.2×10^{-3}	6.5×10^{-3}	1.68×10^{-2}
SOUL	$\mathbf{3 \times 10^{-3}}$	$\mathbf{3 \times 10^{-3}}$	$\mathbf{3 \times 10^{-3}}$

2) Four-layer phantom: The ground truth and the strain estimates corresponding to the four-layer simulation phantom have been reported in Fig. 3. The Hybrid method shows several artifacts, especially in stiff layers. This shows that the several post-processing steps in this method (including a median filter) have not been able to correct for errors in TDE. In addition, this method fails to clearly define the boundaries between tissue regions with different elastic properties. MPWC-Net++ underestimates the strain values in soft layers. Although GLUE strain corresponds well with the ground truth, it is noisy. To reduce the noise, we penalize the displacement variability 15

TABLE II: RMSE corresponding to the strain images obtained from the thin-layer and low-contrast phantoms.

	Thin-layer	Low-contrast
Hybrid	1.37×10^{-2}	5×10^{-3}
GLUE	3.5×10^{-3}	2.7×10^{-3}
MPWC-Net++	3.5×10^{-3}	2.9×10^{-3}
SOUL	$\mathbf{2.3 \times 10^{-3}}$	$\mathbf{9.21 \times 10^{-4}}$

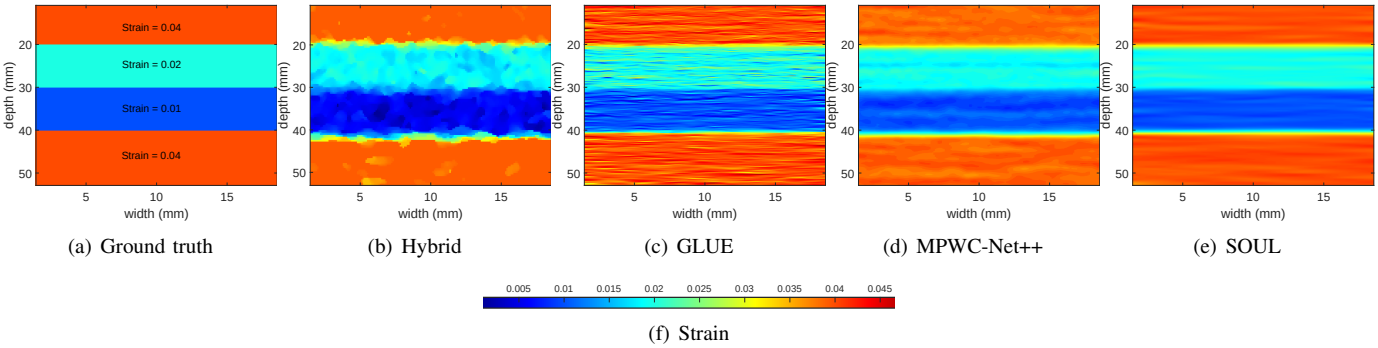

(a) Ground truth (b) Hybrid (c) GLUE (d) MPWC-Net++ (e) SOUL

(f) Strain

Fig. 3: Strain images obtained from the simulation phantom with four layers. Columns 1 to 5 show the ground truth and the axial strain images for Hybrid, GLUE, MPWC-Net++ and SOUL, respectively.

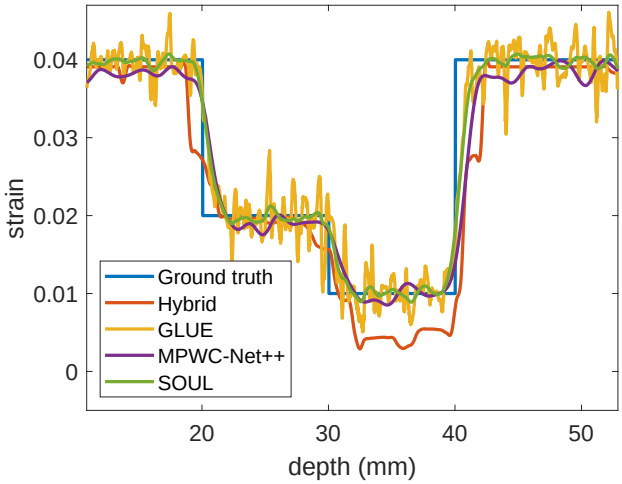

Fig. 4: Strain profile over a vertical line of the simulated phantom with four layers.

times stronger than before. Although the uniform regions exhibit lower variance with this strong regularization, the edges become blurry (Fig. 1(a) of Supplementary Material). SOUL obtains substantially higher quality strain image with smoother background and sharper edges. Due to the short differentiation kernel of length 3 samples only (i.e. 0.06 mm), GLUE strain suffers from noticeable horizontal stripes which are mostly resolved by SOUL. Further reduction of such artifacts can be achieved by increasing the differentiation window size. However, a large differentiation kernel often oversmoothes the strain estimate. To obtain a concrete interpretation of different techniques' performance, in Fig. 4, we plot the ESFs over a vertical line of the ground truth and the estimated strain images. The Hybrid method exhibits slight underestimation of strain in the lower elasticity regions whereas in the region with high elasticity, the deviation from the ground truth is notably large. MPWC-Net++ yields noticeable deviation from the ground truth in the soft layers. The estimation variance of GLUE is evident from the strain plot. SOUL displays the closest match with the ground truth by obtaining a smooth strain profile in the uniform regions and sharp transitions in the boundaries.

To assess the techniques' robustness to scatterer position and amplitude, we report the results for this four-layer phantom corresponding to three random realizations of scatterer position and amplitude. Fig. 5 shows the results for Realization 1. Since the strain images corresponding to all three realizations are similar, we report the results for Realizations 2 and 3 in Fig. 5 of the Supplementary Material. For each case, random Gaussian noise with a Peak SNR (PSNR) value of 20 dB has been added to the RF data. The strain images obtained by Hybrid are extensively noise-corrupted. GLUE suffers from estimation variance in all three cases. MPWC-Net++ yields lower estimation variance than GLUE. However, it fails to recover the true strain in deep tissue regions. SOUL yields consistent performance in all three cases and generates high-quality strain images. The visual superiority of SOUL over other techniques is substantiated by the RMSE values reported in Table I.

3) Thin-layer phantom: Fig. 6 shows the ground truth and axial strain images corresponding to the simulated phantom containing a thin stiff layer. All four techniques successfully identify the stiff layer. Hybrid overestimates strain in the soft layers and exhibits high estimation noise around the stiff layer. Although GLUE strain suffers from several artifacts around the boundary of the stiff layer, it corresponds well with the ground truth. Also, while MPWC-Net++ obtains a smooth strain map, it produces noticeable artifacts in deep tissue regions. Finally, SOUL strain substantially outperforms those obtained by the other three techniques and yields the best visual correspondence with the ground truth which is corroborated by the quantitative values of RMSE reported in Table II.

4) Low-contrast phantom: The axial strain images and the ground truth for the simulated phantom with low elastic contrast between different layers have been reported in Fig. 7. Hybrid fails to recover the stiff layer in this case. GLUE and MPWC-Net++ show good contrast between different layers. However, GLUE exhibits large estimation variance whereas MPWC-Net++ slightly overestimates the strain in certain regions. SOUL yields the best performance in terms of contrast and background smoothness. RMSE values in Table II support this visual interpretation.

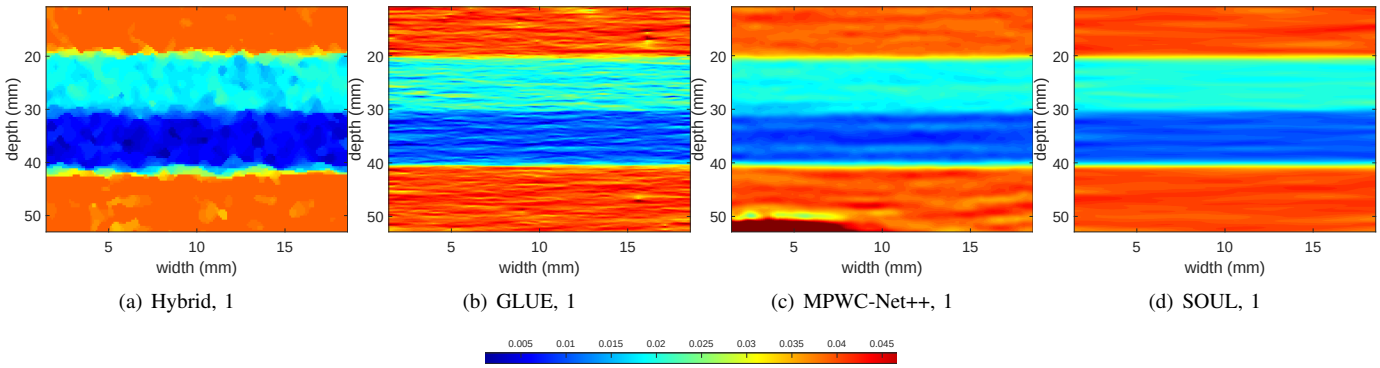

(a) Hybrid, 1 (b) GLUE, 1 (c) MPWC-Net++, 1 (d) SOUL, 1

(e) Strain

Fig. 5: Strain images obtained from Realization 1 of the simulated layer phantom. Columns 1 to 4 correspond to strain images produced by Hybrid, GLUE, MPWC-Net++ and SOUL, respectively. The results for Realizations 2 and 3 are shown in Fig. 5 of the Supplementary Material.

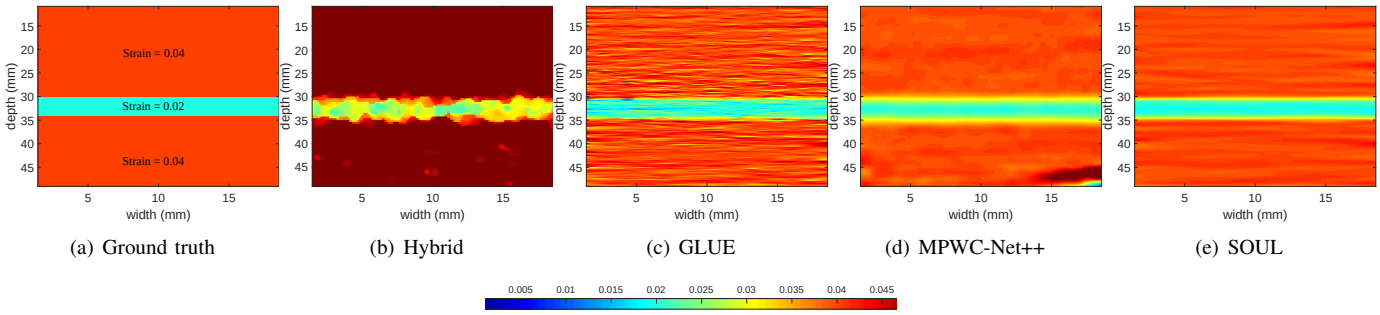

(a) Ground truth (b) Hybrid (c) GLUE (d) MPWC-Net++ (e) SOUL

(f) Strain

Fig. 6: Strain images obtained from the simulation phantom with thin layer. Columns 1 to 5 depict the ground truth and strain images generated by Hybrid, GLUE, MPWC-Net++ and SOUL, respectively.

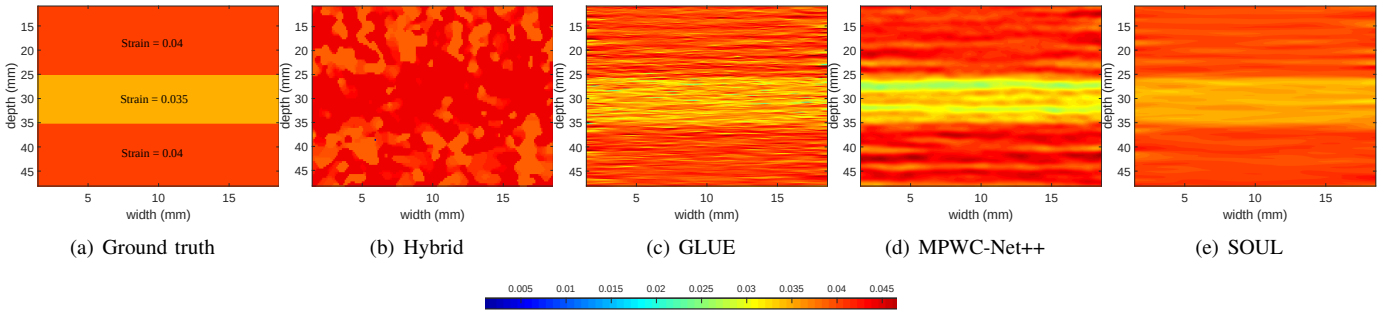

(a) Ground truth (b) Hybrid (c) GLUE (d) MPWC-Net++ (e) SOUL

(f) Strain

Fig. 7: Strain images corresponding to the simulated phantom with low elastic contrast. Columns 1 to 5 show the ground truth and axial strain images obtained from Hybrid, GLUE, MPWC-Net++ and SOUL, respectively.

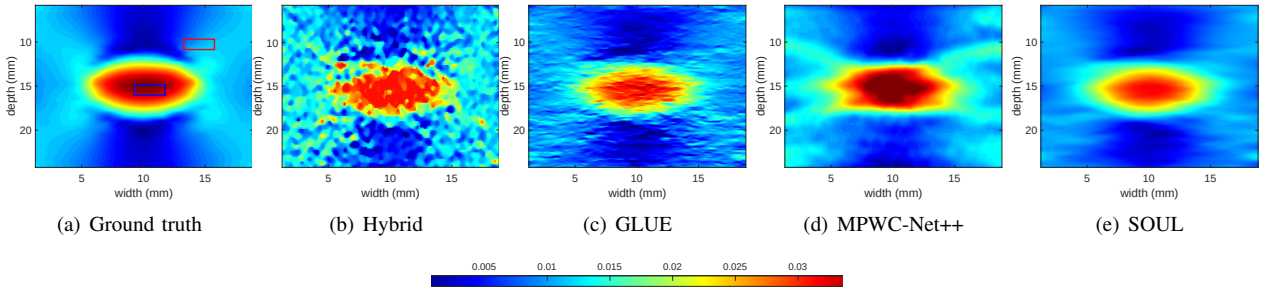

(a) Ground truth (b) Hybrid (c) GLUE (d) MPWC-Net++ (e) SOUL

(f) Strain

Fig. 8: Axial strain images obtained from the soft-inclusion simulation phantom. Column 1 shows the ground truth strain image obtained from FEM. Columns 2 to 5 depict strain images from Hybrid, GLUE, MPWC-Net++ and SOUL, respectively.

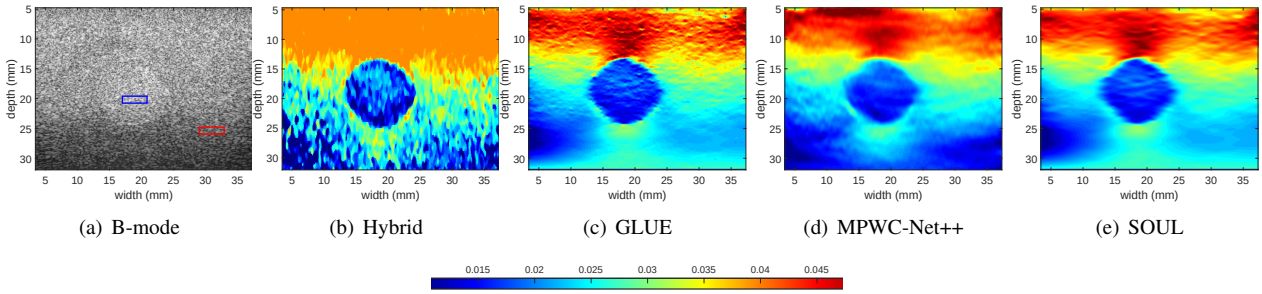

(a) B-mode (b) Hybrid (c) GLUE (d) MPWC-Net++ (e) SOUL

(f) Strain

Fig. 9: Axial strain images generated from the experimental breast elastography phantom. Columns 1 to 5 represent the B-mode image and the strain images from Hybrid, GLUE, MPWC-Net++ and SOUL, respectively.

5) Soft-inclusion phantom: Fig. 8 depicts the strain images obtained from the soft-inclusion simulation phantom. Although the Hybrid method succeeds in discerning the inclusion, the strain image is mostly corrupted by noise. Visually, GLUE outperforms Hybrid by generating a better quality strain image. However, the strain image still shows substantial variability in the uniform tissue regions and the inclusion-background boundary is not satisfactorily defined. MPWC-Net++ obtains smoother strain image than GLUE. However, it exhibits slight distortion of inclusion boundary. SOUL resolves the issues associated with other three techniques and yields the lowest variance estimate of the strain map with a clearly defined edge. The SNR and CNR values reported in Table III corroborate the visual superiority of the proposed technique. It is worth noting that the strain image obtained by SOUL closely resembles the ground truth strain generated using FEM. To investigate whether GLUE achieves a performance similar to SOUL with stronger regularization, we increase the regularization parameter values of GLUE by 10 times. However, this strong regularization over-smoothes the strain image where the boundary is washed-out (Fig. 1(b) of Supplementary Material). In addition, the visual contrast between different elastic areas decreases noticeably.

To represent the quantitative performance of the entire strain image, we select 6 target windows and 20 background windows. For 120 combinations of the target and background windows, we calculate the CNR values which have been employed to obtain the histogram depicted in Fig. 11(a). The histogram shows that SOUL exhibits high frequencies corresponding to the high CNR values. Hybrid, GLUE, MPWC-Net++ and SOUL methods achieve average CNR values of 8.99, 12.22, 15.62 and **19.47**, respectively.

TABLE III: SNR and CNR for the soft-inclusion simulation phantom. CNR is calculated from blue colored target and red colored background windows shown in Fig. 8(a). SNR is calculated on the red colored background window.

	SNR	CNR
Hybrid	3.30	7.81
GLUE	5.52	16.82
MPWC-Net++	6.03	21.25
SOUL	**7.05**	**28.99**

B. Experimental Phantom Results

The B-mode and the strain images obtained from the CIRS breast elastography phantom have been reported in Fig. 9. All four techniques successfully distinguish the hard inclusion from the background. The Hybrid method yields unrealistically uniform strain in the shallow regions whereas the other areas are extensively corrupted by noise stemming from estimation variance. Although GLUE does not suffer from the issue in the shallow regions, it estimates a moderately noisy strain image. In addition, the boundaries of the inclusion are not sharp. We investigate the performance of GLUE with 10 times stronger regularization. In our experience, this high regularization leads

TABLE IV: SNR and CNR for the breast elastography phantom. CNR is calculated using blue colored target and red colored background windows indicated in Fig. 9(a). SNR is calculated using the red colored window on the background.

	SNR	CNR
Hybrid	7.72	1.49
GLUE	54.24	6.20
MPWC-Net++	37.93	8.93
SOUL	**88.17**	**9.55**

to a low-variance estimate by deteriorating the edge sharpness (see Fig. 1(c) of Supplementary Material). Another important observation is that higher regularization leads to a lower visual contrast by decreasing the darkness in the high-elasticity region. MPWC-Net++ obtains a smooth strain map with clearly defined inclusion boundary. However, it underestimates strain in certain tissue regions. SOUL estimates a substantially higher quality strain map than other three techniques by minimizing the variance in the background and maximizing the visual contrast. The quantitative values of SNR and CNR presented in Table IV substantiate our visual assessment of the performance of different techniques. It is worth mentioning that both GLUE and SOUL yield slight stretching of the inclusion in the lateral direction. This might be an effect of the first-order regularization in the lateral domain.

The histogram of CNR values (see Fig. 11(b)) obtained using 120 combinations of 6 target and 20 background windows shows that the high CNR values belong mostly to SOUL. Here, Hybrid exhibits the highest frequency of the low CNR values. Quantitatively, the four techniques under consideration namely Hybrid, GLUE, MPWC-Net++ and SOUL yield average CNR values of 4.42, 9, 8.16 and **12.87**, respectively.

C. In vivo Liver Cancer Results

Fig. 10 depicts the B-mode and the strain images generated using the *in vivo* datasets from two patients with liver cancer. For Patient 1, GLUE, MPWC-Net++ and SOUL show good contrast between the tumor and normal tissue. However, the tumor is hardly visible in the strain image obtained by the Hybrid method. In case of Patient 2, all four techniques succeed in distinguishing the tumor from the healthy tissue. Hybrid exhibits better performance in Patient 2 than that in Patient 1. This discrepancy in performance of Hybrid might be caused by the presence of a blood vessel in the field-of-view of the first *in vivo* data. The easily deformable blood vessel yields notably higher strain than the surrounding tissue. Due to the consideration of neighboring samples during displacement estimation, the surrounding tissue strains are affected by the samples representing the vessel. This mutual effect results in an irregular distribution of high strain values, yielding a noisy appearance of the strain image. Although GLUE visually outperforms Hybrid, it still suffers from variability in the background where the edges are not satisfactorily defined. Increasing the regularization weights by 10 times smoothens the background by further reduction of the boundary sharpness while sacrificing tumor darkness (see Figs. 1(d) and 1(e) of Supplementary Material). MPWC-Net++ exhibits extensive background noise in case of Patient 1 whereas it distorts the tumor boundary of Patient 2. Besides, it underestimates the strain in deep tissue regions of Patient 1. In both patient cases, SOUL substantially outperforms Hybrid, GLUE and MPWC-Net++ by presenting lowest variance in the background and highest clarity of edges. It is worth mentioning that SOUL exhibits high level of smoothing in certain regions of Fig. 10(j). This might happen due to low echogenicity in certain regions of the RF data where regularization dominates data similarity. However, SOUL manifests notably better target-background contrast than the other techniques. This visual inference is quantitatively validated by the SNR and CNR values reported in Table V.

TABLE V: SNR and CNR of the strain images obtained from *in vivo* liver datasets. CNR values are calculated between blue colored target and red colored background windows depicted in Figs. 10(a) and 10(f). SNR values are calculated on the red colored background windows.

	Patient 1		Patient 2	
	SNR	CNR	SNR	CNR
Hybrid	4.71	2.62	12.89	7.15
GLUE	18.25	14.73	23.28	8.77
MPWC-Net++	29.35	18.98	18.58	7.33
SOUL	**33.10**	**24.33**	**37.60**	**14.35**

The histograms of CNR values across the entire strain images corresponding to Patients 1 and 2 have been reported in Figs. 11(c) and 11(d), respectively. In both cases, SOUL exhibits the highest frequency in high CNR values. Aligned with the visual interpretation, the Hybrid method shows higher frequency in low CNR values. Hybrid, GLUE, MPWC-Net++ and SOUL methods yield average CNR values of 2.86, 14.02, 11.40 and **21.61** for Patient 1 and 7.37, 7.80, 9.89 and **10.35** for Patient 2, respectively.

D. Computation Time

Hybrid, GLUE and SOUL have been implemented on MATLAB R2018b platform using an 8^{th} generation Intel core-i7 CPU clocked at 3.2 GHz. MPWC-Net++ have been executed on an NVIDIA TITAN V GPU with 12 GB memory. Times required by Hybrid, GLUE, MPWC-Net++ and SOUL to calculate the displacement field between two RF frames of size 1000×100 are reported in Table VI. Hybrid requires the highest execution time. The runtime of SOUL is higher than that of GLUE due to the additional blocks stemming from the second-order continuity constraint. An optimized implementation on a GPU can expedite the execution of SOUL. MPWC-Net++ requires the lowest running time. However, this technique demands extensive amount of memory and time in the training phase.

V. Discussion

The proposed regularization term based on the second-order derivative of the displacement does not penalize affine changes in the displacement field. As such, it leads to a much

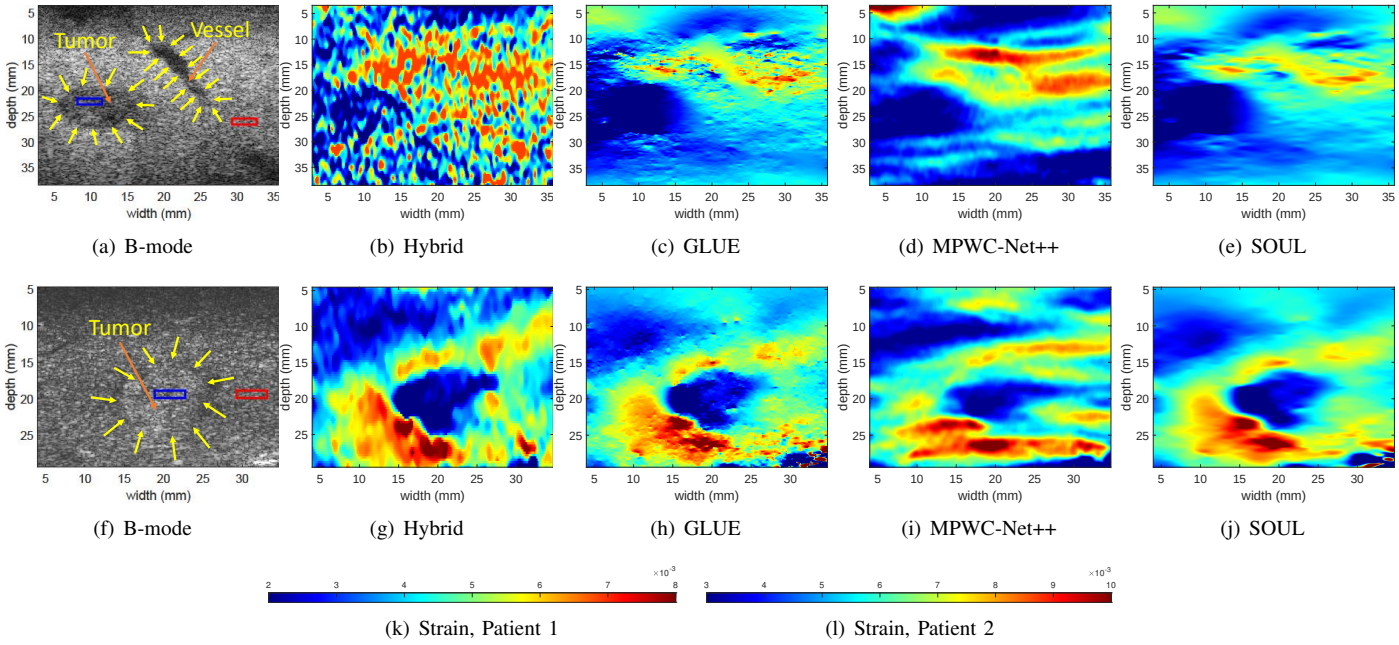

(a) B-mode (b) Hybrid (c) GLUE (d) MPWC-Net++ (e) SOUL

(f) B-mode (g) Hybrid (h) GLUE (i) MPWC-Net++ (j) SOUL

(k) Strain, Patient 1 (l) Strain, Patient 2

Fig. 10: *In vivo* results obtained from the liver patients. Rows 1 and 2 correspond to Patients 1 and 2, respectively. Column 1 shows the B-mode images. Columns 2 to 5 represent the axial strain images corresponding to Hybrid, GLUE, MPWC-Net++ and SOUL, respectively.

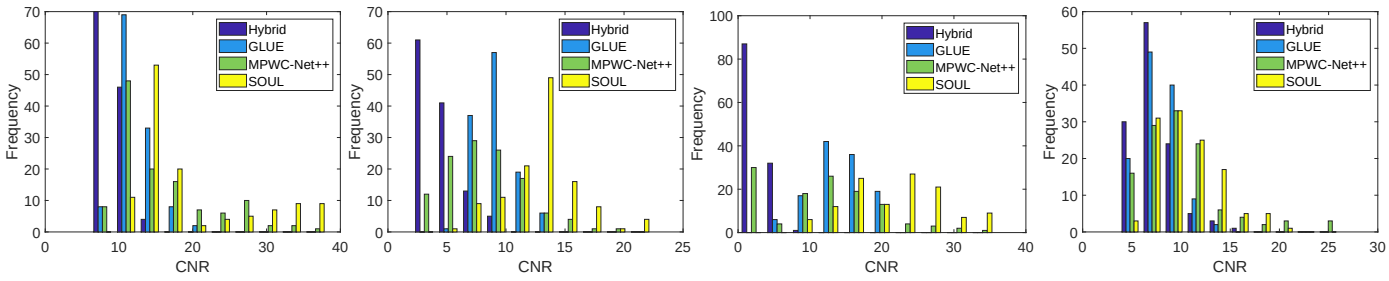

(a) Soft-inclusion simulation phantom (b) Experimental phantom (c) *In vivo* liver data, Patient 1 (d) *In vivo* liver data, Patient 2

Fig. 11: Histograms of the CNR values obtained using 120 combinations of target and background windows. Columns 1 to 4 depict the histograms corresponding to the simulated phantom with soft inclusion, experimental breast elastography phantom, *in vivo* liver data from Patients 1 and 2, respectively.

TABLE VI: Runtime for calculating displacement between RF frames of size 1000×100. MPWC-Net++ runs on a GPU and the rest of the methods run on a CPU.

	Time (seconds)
Hybrid	21.80
GLUE	0.58
MPWC-Net++	**0.09**
SOUL	1.28

smaller estimation bias compared to GLUE, which enforces the displacement field to be constant. This is confirmed in our simulation and experimental results.

In certain cases, the strain in the tissue gradually decreases with depth due to stress dissipation, where top layers undergo maximum amount of stress while the stress decreases with depth as a result of stress propagation over increasingly larger areas with depth. The first-order continuity constraint alone fails to optimally estimate the strain in such situations (see Fig. 2). With moderate regularization, the estimated strain shows extensive variability around the true strain whereas the curve tends to flatten with increasing regularization. As the results suggest, a combination of first- and second-order spatial derivative constraints handle this situation well and obtains a strain profile close to the ground truth.

In different examples presented in this investigation, the continuity weights of GLUE were set to different values to determine whether GLUE can achieve the performance of SOUL depending on the level of regularization. It was observed that strong regularization smoothens the strain image with a substantial loss of both visual contrast and bound-

ary sharpness. In contrast, SOUL imposes both second and adaptive first-order continuity constraints which fully align with tissue deformation physics. This realistic model of the deformation field drives SOUL strain to converge to the correct value. As a result, SOUL obtains a spatially smooth strain map maintaining edge clarity and visual contrast. Since SOUL takes advantage of higher-order spatial continuity, it yields better noise suppression than previous techniques. However, this higher level of noise suppression might introduce over-smoothing to the estimated strain. This potential drawback can be mitigated by utilizing $l1$ norm of the second-order continuity terms instead of $l2$ norm. In addition, sample-wise regularization scheme can be adopted to maintain proper balance between displacement continuity and discontinuity. However, these extensions are beyond the scope of this work while being interesting avenues of future work. SOUL takes only the amplitude constancy into account to construct the data term. However, amplitude constancy alone is not sufficient to oversee the outlier RF samples. An adaptive combination of amplitude and gradient similarity constraints [40] can potentially make the data function robust to outliers.

Different factors might affect the optimality of the regularization parameter values. Optimal combination of the continuity weights is mainly controlled by the organ's quantitative properties such as attenuation coefficient, the size and distribution of the scatterers, etc. In addition, imaging parameters such as transmit and temporal sampling frequencies also play a crucial role in determining the optimal parameter set. Furthermore, the level of acquisition noise and temporal characteristics of the deformation field also affect the parameter values. In this work, the optimal regularization parameters were obtained using an ad hoc method where the quality of the strain images corresponding to different parameter sets were assessed visually to select the best one. Another option involves using the well-known L-curve [55] technique for their automatic selection. It is important to note that these optimal values do not need to be tuned for every pair of images. They should be tuned with new organs imaged with a different imaging setting. However, due to the presence of more than one continuity weights, the L-curve technique will involve extensive amount of calculation. Another potential approach can be generating displacement images using different sets of parameters and devising a feature-based classifier to choose the displacement of each sample individually from different options stemming from different weights. However, this machine learning-based option would require extensive amount of training datasets. It is noteworthy that the TDE results are minimally sensitive to even a 50% increase in all regularization weights.

VI. Conclusion

A novel regularized-optimization based ultrasound elastography technique called SOUL is proposed in this paper. We have formulated a cost function containing the data term, and the first- and second-order continuity terms. The newly introduced second-order regularization term leads to a substantially better quality strain image with smooth background and sharp edges. We analytically optimize the aforementioned non-linear penalty function in an efficient manner and obtain a system of linear equations which is solved for more than a million variables in less than 1.5 seconds while working with conventional ultrasound RF frames. Extensive validation against simulation, phantom and *in vivo* liver cancer datasets proves the proposed technique's potential in high quality strain imaging.

Acknowledgment

This work has been supported by Natural Sciences and Engineering Research Council of Canada (NSERC) RGPIN-2020-04612. Authors thank Drs. E. Boctor, M. Choti and G. Hager for allowing us to use the liver data. We thank Dr. M. K. Hasan for sharing the code of the Hybrid method, and Dr. A. Nahiyan for helping us fine-tune the code for our data. We also thank Mr. A. K. Z. Tehrani for his valuable discussions. Authors thank the anonymous reviewers for their constructive feedback.

References

[1] H. Karimi, A. Fenster, and A. Samani, "A novel fast full inversion based breast ultrasound elastography technique," *Physics in Medicine & Biology*, vol. 58, no. 7, p. 2219, 2013.

[2] T. J. Hall, Y. Zhu, and C. S. Spalding, "In vivo real-time freehand palpation imaging," *Ultrasound in medicine & biology*, vol. 29, no. 3, pp. 427–435, 2003.

[3] A. Nahiyan and M. K. Hasan, "Hybrid algorithm for elastography to visualize both solid and fluid-filled lesions," *Ultrasound in Medicine & Biology*, vol. 41, no. 4, pp. 1058 – 1078, 2015.

[4] O. Falou, A. Sadeghi-Naini, S. Prematilake, E. Sofroni, N. Papanicolau, S. Iradji, Z. Jahedmotlagh, S. Lemon-Wong, J.-P. Pignol, E. Rakovitch *et al.*, "Evaluation of neoadjuvant chemotherapy response in women with locally advanced breast cancer using ultrasound elastography," *Translational oncology*, vol. 6, no. 1, pp. 17–24, 2013.

[5] H. Rivaz, E. M. Boctor, M. A. Choti, and G. D. Hager, "Real-time regularized ultrasound elastography," *IEEE Transactions on Medical Imaging*, vol. 30, no. 4, pp. 928–945, 2011.

[6] H. Rivaz, I. Fleming, L. Assumpcao, G. Fichtinger, U. Hamper, M. Choti, G. Hager, and E. Boctor, "Ablation monitoring with elastography: 2d in-vivo and 3d ex-vivo studies," in *International Conference on Medical Image Computing and Computer-Assisted Intervention*, 2008, pp. 458–466.

[7] S. Bharat, U. Techavipoo, M. Z. Kiss, W. Liu, and T. Varghese, "Monitoring stiffness changes in lesions after radiofrequency ablation at different temperatures and durations of ablation," *Ultrasound in medicine & biology*, vol. 31, no. 3, pp. 415–422, 2005.

[8] T. Varghese, J. Zagzebski, P. Rahko, and C. Breburda, "Ultrasonic imaging of myocardial strain using cardiac elastography," *Ultrasonic imaging*, vol. 25, no. 1, pp. 1–16, 2003.

[9] E. E. Konofagou, J. D'hooge, and J. Ophir, "Myocardial elastography—a feasibility study in vivo," *Ultrasound in medicine & biology*, vol. 28, no. 4, pp. 475–482, 2002.

[10] J. Luo, K. Fujikura, S. Homma, and E. E. Konofagou, "Myocardial elastography at both high temporal and spatial resolution for the detection of infarcts," *Ultrasound in medicine & biology*, vol. 33, no. 8, pp. 1206–1223, 2007.

[11] J. D'hooge, A. Heimdal, F. Jamal, T. Kukulski, B. Bijnens, F. Rademakers, L. Hatle, P. Suetens, and G. R. Sutherland, "Regional strain and strain rate measurements by cardiac ultrasound: principles, implementation and limitations," *European Journal of Echocardiography*, vol. 1, no. 3, pp. 154–170, 2000.

[12] J. D'hooge, B. Bijnens, J. Thoen, F. Van de Werf, G. R. Sutherland, and P. Suetens, "Echocardiographic strain and strain-rate imaging: a new tool to study regional myocardial function," *IEEE transactions on medical imaging*, vol. 21, no. 9, pp. 1022–1030, 2002.

[13] R. L. Maurice, G. Soulez, M.-F. Giroux, and G. Cloutier, "Noninvasive vascular elastography for carotid artery characterization on subjects without previous history of atherosclerosis," *Medical physics*, vol. 35, no. 8, pp. 3436–3443, 2008.

[14] H. Li, J. Porée, B. Chayer, M.-H. R. Cardinal, and G. Cloutier, "Parameterized strain estimation for vascular ultrasound elastography with sparse representation," *IEEE Trans. Medical Imaging*, 2020.

[15] C. Huang, Q. He, M. Huang, L. Huang, X. Zhao, C. Yuan, and J. Luo, "Non-invasive identification of vulnerable atherosclerotic plaques using texture analysis in ultrasound carotid elastography: An in vivo feasibility study validated by magnetic resonance imaging," *Ultrasound in Medicine & Biology*, vol. 43, no. 4, pp. 817–830, 2017.

[16] J. Luo and E. E. Konofagou, "A fast normalized cross-correlation calculation method for motion estimation," *IEEE trans. ultrasonics, ferroelectrics, and freq. control*, vol. 57, no. 6, pp. 1347–1357, 2010.

[17] C. L. De Korte and A. F. Van Der Steen, "Intravascular ultrasound elastography: an overview," *Ultrasonics*, vol. 40, no. 1-8, pp. 859–865, 2002.

[18] J. A. Schaar, C. L. de Korte, F. Mastik, C. Strijder, G. Pasterkamp, E. Boersma, P. W. Serruys, and A. F. van der Steen, "Characterizing vulnerable plaque features with intravascular elastography," *Circulation*, vol. 108, no. 21, pp. 2636–2641, 2003.

[19] S. R. Mousavi, A. Sadeghi-Naini, G. J. Czarnota, and A. Samani, "Towards clinical prostate ultrasound elastography using full inversion approach," *Medical physics*, vol. 41, no. 3, p. 033501, 2014.

[20] J.-L. Gennisson, N. Grenier, C. Combe, and M. Tanter, "Supersonic shear wave elastography of in vivo pig kidney: influence of blood pressure, urinary pressure and tissue anisotropy," *Ultrasound in medicine & biology*, vol. 38, no. 9, pp. 1559–1567, 2012.

[21] Y. Wang, M. Bayer, J. Jiang, and T. J. Hall, "An improved region-growing motion tracking method using more prior information for 3-d ultrasound elastography," *IEEE Transactions on Ultrasonics, Ferroelectrics, and Frequency Control*, vol. 67, no. 3, pp. 580–597, 2020.

[22] F.-F. Lee, Q. He, and J. Luo, "Electromagnetic tracking-based freehand 3d quasi-static elastography with 1d linear array: a phantom study," *Physics in Medicine & Biology*, vol. 63, no. 24, p. 245006, 2018.

[23] S. R. Ara, F. Mohsin, F. Alam, S. A. Rupa, S. Y. Lee, M. K. Hasan, and R. Awwal, "Phase-based direct average strain estimation for elastography," *IEEE Transactions on Ultrasonics, Ferroelectrics, and Frequency Control*, vol. 60, no. 11, pp. 2266–2283, 2013.

[24] M. Mirzaei, A. Asif, M. Fortin, and H. Rivaz, "3d normalized cross-correlation for estimation of the displacement field in ultrasound elastography," *Ultrasonics*, vol. 102, p. 106053, 2020.

[25] J. Bamber, D. Cosgrove, C. Dietrich, J. Fromageau, J. Bojunga, F. Calliada, V. Cantisani, J.-M. Correas, M. D'onofrio, E. Drakonaki *et al.*, "Efsumb guidelines and recommendations on the clinical use of ultrasound elastography. part 1: Basic principles and technology," *Ultraschall in der Medizin-European Journal of Ultrasound*, vol. 34, no. 02, pp. 169–184, 2013.

[26] S. K. Alam, J. Ophir, and T. Varghese, "Elastographic axial resolution criteria: An experimental study," *IEEE transactions on ultrasonics, ferroelectrics, and frequency control*, vol. 47, no. 1, pp. 304–309, 2000.

[27] M. G. Kibria and H. Rivaz, "Gluenet: Ultrasound elastography using convolutional neural network," in *Simulation, Image Processing, and Ultrasound Systems for Assisted Diagnosis and Navigation*, 2018, pp. 21–28.

[28] Z. Gao, S. Wu, Z. Liu, J. Luo, H. Zhang, M. Gong, and S. Li, "Learning the implicit strain reconstruction in ultrasound elastography using privileged information," *Medical image analysis*, vol. 58, p. 101534, 2019.

[29] S. Wu, Z. Gao, Z. Liu, J. Luo, H. Zhang, and S. Li, "Direct reconstruction of ultrasound elastography using an end-to-end deep neural network," in *International Conference on Medical Image Computing and Computer-Assisted Intervention*. Springer, 2018, pp. 374–382.

[30] A. K. Z. Tehrani and H. Rivaz, "Displacement estimation in ultrasound elastography using pyramidal convolutional neural network," *IEEE Transactions on Ultrasonics, Ferroelectrics, and Frequency Control*, vol. 67, no. 12, pp. 2629–2639, 2020.

[31] A. K. Z. Tehrani, M. Amiri, and H. Rivaz, "Real-time and high quality ultrasound elastography using convolutional neural network by incorporating analytic signal," in *IEEE EMBC)*, 2020, pp. 2075–2078.

[32] R. M. Pohlman and T. Varghese, "Dictionary representations for electrode displacement elastography," *IEEE trans. ultrasonics, ferroelectrics, and frequency control*, vol. 65, no. 12, pp. 2381–2389, 2018.

[33] A. Zayed and H. Rivaz, "Fast strain estimation and frame selection in ultrasound elastography using machine learning," *IEEE Transactions on Ultrasonics, Ferroelectrics, and Frequency Control*, 2020.

[34] M. Ashikuzzaman and H. Rivaz, "Denoising rf data via robust principal component analysis: Results in ultrasound elastography," in *2020 42nd Annual International Conference of the IEEE Engineering in Medicine Biology Society (EMBC)*, 2020, pp. 2067–2070.

[35] N. Gokhale, M. Richards, A. Oberai, P. Barbone, and M. Doyley, "Simultaneous elastic image registration and elastic modulus reconstruction," in *2004 2nd IEEE International Symposium on Biomedical Imaging: Nano to Macro*, 2004, pp. 543–546.

[36] J. Jiang and T. J. Hall, "A generalized speckle tracking algorithm for ultrasonic strain imaging using dynamic programming," *Ultrasound in Medicine & Biology*, vol. 35, no. 11, pp. 1863 – 1879, 2009.

[37] H. S. Hashemi and H. Rivaz, "Global time-delay estimation in ultrasound elastography," *IEEE Transactions on Ultrasonics, Ferroelectrics, and Frequency Control*, vol. 64, no. 10, pp. 1625–1636, 2017.

[38] M. Ashikuzzaman, C. J. Gauthier, and H. Rivaz, "Global ultrasound elastography in spatial and temporal domains," *IEEE Transactions on Ultrasonics, Ferroelectrics, and Frequency Control*, vol. 66, no. 5, pp. 876–887, 2019.

[39] M. Ashikuzzaman and H. Rivaz, "Incorporating multiple observations in global ultrasound elastography," in *2020 42nd Annual International Conference of the IEEE Engineering in Medicine Biology Society (EMBC)*, 2020, pp. 2007–2010.

[40] M. Ashikuzzaman, T. J. Hall, and H. Rivaz, "Adaptive data function for robust ultrasound elastography," in *2020 IEEE International Ultrasonics Symposium (IUS), in press*, pp. 1–4.

[41] Q. Zhang, C. Li, M. Zhou, Y. Liao, C. Huang, J. Shi, Y. Wang, and W. Wang, "Quantification of carotid plaque elasticity and intraplaque neovascularization using contrast-enhanced ultrasound and image registration-based elastography," *Ultrasonics*, vol. 62, pp. 253–262, 2015.

[42] X. Pan, K. Liu, J. Shao, J. Gao, L. Huang, J. Bai, and J. Luo, "Performance comparison of rigid and affine models for motion estimation using ultrasound radio-frequency signals," *IEEE Transactions on Ultrasonics, Ferroelectrics, and Frequency Control*, vol. 62, no. 11, pp. 1928–1943, 2015.

[43] M. Mirzaei, A. Asif, and H. Rivaz, "Combining total variation regularization with window-based time delay estimation in ultrasound elastography," *IEEE Transactions on Medical Imaging*, vol. 38, no. 12, pp. 2744–2754, 2019.

[44] N. Kheirkhah, S. C. H. Dempsey, H. Rivaz, A. Samani, and A. Sadeghi-Naini, "A tissue mechanics based method to improve tissue displacement estimation in ultrasound elastography," in *IEEE EMBC*, 2020.

[45] H. Rivaz, E. Boctor, P. Foroughi, R. Zellars, G. Fichtinger, and G. Hager, "Ultrasound elastography: A dynamic programming approach," *IEEE Transactions on Medical Imaging*, vol. 27, no. 10, pp. 1373–1377, 2008.

[46] M. Ashikuzzaman, C. Belasso, M. G. Kibria, A. Bergdahl, C. J. Gauthier, and H. Rivaz, "Low rank and sparse decomposition of ultrasound color flow images for suppressing clutter in real-time," *IEEE Transactions on Medical Imaging*, vol. 39, no. 4, pp. 1073–1084, 2020.

[47] A. K. Z. Tehrani and H. Rivaz, "Mpwc-net++: Evolution of optical flow pyramidal convolutional neural network for ultrasound elastography," in *SPIE Medical Imaging*, 2021.

[48] J. Jensen, "Field: A program for simulating ultrasound systems," *Medical and Biological Engineering and Computing*, vol. 34, pp. 351–352, 1996.

[49] M. K. Hasan, E. M. A. Anas, S. K. Alam, and S. Y. Lee, "Direct mean strain estimation for elastography using nearest-neighbor weighted least-squares approach in the frequency domain," *Ultrasound in medicine & biology*, vol. 38, no. 10, pp. 1759–1777, 2012.

[50] D. Sun, X. Yang, M. Liu, and J. Kautz, "Pwc-net: Cnns for optical flow using pyramid, warping, and cost volume," in *2018 IEEE/CVF Conf. on Computer Vision and Pattern Recog.*, 2018, pp. 8934–8943.

[51] J. Hur and S. Roth, "Iterative residual refinement for joint optical flow and occlusion estimation," in *Proceedings of the IEEE Conference on Computer Vision and Pattern Recognition*, 2019, pp. 5754–5763.

[52] F. Kallel and J. Ophir, "A least-squares strain estimator for elastography," *Ultrasonic imaging*, vol. 19, no. 3, pp. 195–208, 1997.

[53] T. Varghese and J. Ophir, "A theoretical framework for performance characterization of elastography: The strain filter," *IEEE Trans. UFFC*, vol. 44, no. 1, pp. 164–172, 1997.

[54] J. Ophir, S. K. Alam, B. Garra, F. Kallel, E. Konofagou, T. Krouskop, and T. Varghese, "Elastography: ultrasonic estimation and imaging of the elastic properties of tissues," *Proceedings of the Institution of Mechanical Engineers, Part H: Journal of Engineering in Medicine*, vol. 213, no. 3, pp. 203–233, 1999.

[55] P. C. Hansen, "The l-curve and its use in the numerical treatment of inverse problems," 1999.